

Electroweak corrections to Higgs boson production via W W fusion at the future LHeC

Bowen Wang,^{1,2,*} Kai Wang,^{1,†} and Hanying Xiong^{1,‡}

¹*Zhejiang Institute of Modern Physics and School of Physics,
Zhejiang University, Hangzhou, Zhejiang 310027, China*

²*School of Physics, Hangzhou Normal University, Hangzhou, Zhejiang 311121, China*

Precision measurement of quark Yukawa couplings is a crucial aspect of Higgs property study. Proposed as a future upgrade of the Large Hadron Collider (LHC), the Large Hadron electron Collider (LHeC) provides opportunities to probe quark Yukawa couplings with a high precision because of relatively low rate from the QCD background as compared with that of the Higgs processes at the LHC. For this purpose, it is important to have a precision prediction of the Higgs production rate at the LHeC. The leading production channel of the Higgs boson at the LHeC is via weak boson fusion (WBF) which has the unique kinematic feature of forward tagging jets. As QCD corrections are suppressed by the simple color structure of the process, electroweak radiative corrections become particularly important. In this paper, we focus on the electroweak radiative corrections at next-to-leading order for the Higgs-boson production via charge current WBF processes at the LHeC. In the two renormalization schemes we use, the loop corrections are respectively at the level of 9% and 18% relative to the leading order result, for a center-of-mass energy at 1.98 TeV, and the next-to-leading order results in both schemes agree up to a truncation error expected from the perturbative method. The size of the EW corrections exceeds that from QCD radiations and is shown to be important for the study of Higgs phenomenology.

I. Introduction

Enormous efforts have been made to study the properties of the 125 GeV Higgs boson at an increasing precision level since its discovery [1, 2]. In particular, the measurement of Higgs couplings to various particles [3–5] is an important part of the endeavor. Recent experiments have achieved a percent level accuracy in the extraction of Higgs couplings to gauge bosons and the top quark [6, 7], which are all in agreement with the standard model (SM) predictions. These measurements are preferably carried out in the leptonic decay channels of the Higgs boson. For instance, in Ref. [7] the Higgs coupling to the Z boson is extracted from $H \rightarrow ZZ^* \rightarrow 4$ leptons; the top quark Yukawa is measured via the Higgs production associated with a top quark pair, with $H \rightarrow$ leptons.

In contrast, the hadronic final states from Higgs decays are much more difficult to probe because of the large rate for the background jets (produced not via intermediate Higgs bosons). The $H \rightarrow \tau^+\tau^-$ with subsequent hadronic decays produces narrow τ jets, but the jet shape alone is insufficient for identifying the process from the hadronic background. Nonetheless, constraining of H - τ Yukawa coupling can be carried out in a production mode commonly referred to as the “weak boson fusion” (WBF), where a pair of intermediate W or Z bosons is radiated by the colliding fermions and couples to a Higgs. The energetic incoming particles evolve to a final state with a pair of fermions (at the parton level) separated by a large rapidity gap, in association with the Higgs and other particles produced in the central rapidity region. The transverse momenta of the two fermions are of order the weak boson mass. This configuration of event is successfully utilized for suppressing backgrounds in the search of $H \rightarrow \tau\tau$ at the Large Hadron Collider (LHC), for both hadronic and leptonic decays of τ 's [8, 9].

The identification of H - b and H - c couplings via WBF at hadron colliders gets even more challenging [10, 11] because of the huge QCD multi-jet background. On the other hand, the Large Hadron electron Collider (LHeC) [12] is proposed partly to measure Higgs couplings such as H - b and H - c . In this upgrade option for the LHC, a beam of electrons will be aligned to collide with the 7 TeV protons. The electron beam energy is considered to range in 50-200 GeV, making the facility a factory to produce Higgs bosons mainly via WBF. Studies have shown the prospect of making the measurement of Yukawa couplings at the LHeC, based on the analysis using leading order (LO) matrix elements in the simulations [12–15]. An account for the next-to-leading order (NLO) corrections is needed both for a precise knowledge of the signal cross section and for determination of various selection criteria affected by the distortion of distributions at NLO.

Computation of NLO QCD and (part of) QED corrections for WBF production of the Higgs has been performed by Blumlein [16], and Jager [17]. The QCD corrections to the total cross section are shown to be at the level of a few percent, while their impact on differential distributions is found to be more sizable, i.e. as large as 10% \sim 20%. The dominant QED radiative corrections are about -5%. As we will show, it is important to include all the NLO EW processes, which give rise to substantial

*Electronic address: bowenw@hznu.edu.cn

†Electronic address: wangkai1@zju.edu.cn

‡Electronic address: 21736003@zju.edu.cn

corrections in both integrated cross section and differential distributions.

We note that part of the EW loop effect has been calculated in a study [18] to estimate the significance of the triple Higgs-self coupling at the LHeC. However, the calculation only involves a small subset of the loop diagrams associated with the coupling. We shall see that the background (with no Higgs self coupling) cross section in this study can be reduced by including all EW loop processes, which makes a negative contribution and therefore yields a better constraint on the Higgs self coupling.

In this paper we present a calculation of the full NLO EW corrections to the WBF cross section in e - p collisions. To make the discussion general we consider only the partonic scattering amplitude with an on-shell Higgs, and do not simulate the final state to which the Higgs decays. For simplicity, the focus will be on the charge current(CC) WBF, which is dominant over the neutral current(NC) process.¹ Moreover, the outgoing electron of the NC process could be tagged in a broad kinematical region where it could be distinguished from the CC process.

The past two decades have seen the fast development of automation programs for the calculation of QCD and EW corrections for various scattering processes at one loop accuracy [19–25]. However, these tools prioritize the processes in p - p and e^+e^- scatterings, and to our best knowledge, no implementation is made as yet in the publicly available Monte-Carlo programs to fully automatize the NLO calculation for e - p collisions. To treat the WBF process at the LHeC, we need to organize different parts of the calculation on our own. The calculation proceeds in the dipole subtraction formalism [26], first designed for a unified treatment of various singularities encountered in scattering amplitudes with real and virtual QCD radiations. The method was then adapted to the calculation of QED radiative corrections and generalized to include the radiative effect that is sensitive to the mass of the initial or final fermions [27–29]. We shall show how to consistently include the fermion mass effect in our calculation of the WBF process using the dipole method.

The rest of the paper is organized as follows. In Sec. II, we give the description of the details for the analytical and numerical parts of the calculation. In Sec. III, we discuss the numerical significance of the NLO EW corrections in both total and differential cross sections of the WBF process. Then we conclude the paper in Sec. IV.

II. Detailed calculation of the process

A. LO contribution

The CC WBF $ep \rightarrow \nu_e j H$ is depicted at the leading order by the partonic process $eq \rightarrow \nu_e q' H$. An example diagram is shown in Fig. 1. The cross section is given by

$$\sigma^{LO} = \sum_q \int_0^1 d\eta_q f_q(\eta_q, \mu_F) \frac{1}{2\hat{s}} d\Phi_3 B(P_A, p_q), \quad (1)$$

where $B(P_A, p_q)$ denotes the born amplitude squared at the parton level with the incoming electron and quark momenta P_A and p_q . The partonic center-of-mass (CM) energy squared is given by $\hat{s} = (P_A + p_q)^2$, and $d\Phi_3$ is the phase space element of the 3-body final state. In this paper we assume no particular polarization for external particles, so that in $B(P_A, p_q)$ and all other squared amplitudes below, we sum and average over colors and spins of the initial and final states. η_q is the fraction of the proton momentum P_B carried by the incoming quark q . The hadronic cross section is factorized at the scale μ_F into a quark distribution function $f_q(\eta_b, \mu_F)$, convolved with a squared hard scattering amplitude depending implicitly on η_q . The evolution of $f_q(\eta_b, \mu_F)$ introduces NLO QCD and QED terms to the LO cross section, which is not a problem as long as we do not double count these terms in our NLO calculation. The dominant contribution comes from the initial quark flavors u , c , \bar{d} and \bar{s} , while the effect of \bar{b} and t is marginal and neglected.

¹ The integrated cross section of CC WBF is about 5 times that of NC WBF at the energy regime of the LHeC.

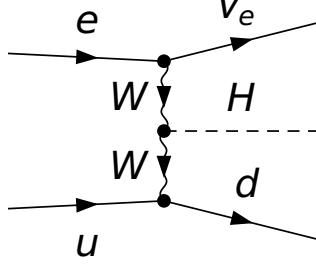


FIG. 1: A representative leading order diagram for CC WBF at the LHeC.

B. NLO EW corrections

The numerically dominant NLO EW corrections are from the loop diagrams of various topologies, ranging from self energy graphs to pentagons. Soft and collinear singularities may arise in some of these diagrams when photons are present in the loop. Representative loop diagrams with and without these singularities are shown in Fig. 3 and Fig. 2, respectively.

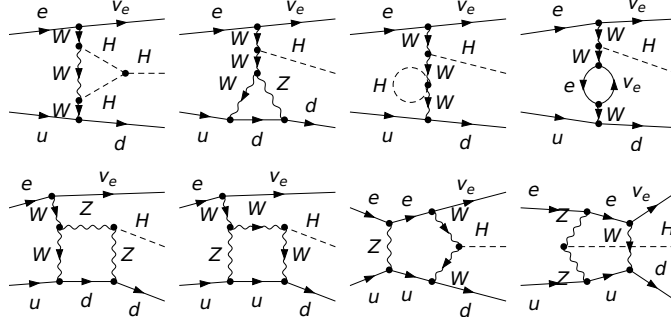


FIG. 2: Representative 1-loop diagrams for CC WBF at the LHeC with no soft/collinear divergences.

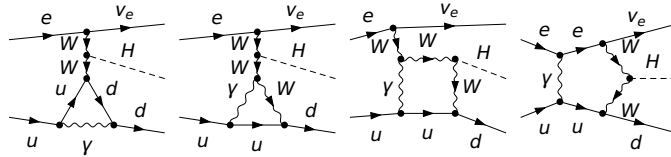


FIG. 3: Representative 1-loop diagrams for CC WBF at the LHeC with soft/collinear divergences.

A consistent treatment of the singularities requires the inclusion of all diagrams with real emission of photons, whose momenta can potentially be either soft or collinear to the emitter. In properly defined observables, cancellation of part of the singularities takes place between real-emission and loop diagrams. Mass singularities associated with initial state radiations are removed by the collinear counter terms provided by the factorization procedure, to be discussed below. There are also real-emission processes induced by photons that are treated as constituents of the initial state protons. In this case, no corresponding loop diagrams are present and the singular terms are cancelled solely by the collinear counter terms.

Within the energy range of the LHeC, we treat u , d , s , and c (and their anti-particles) as massless flavors, whose couplings with the Higgs are also neglected. The contribution from b and t (and their anti-particles) is marginal and not included. The role of the electron mass is somewhat intricate and will be discussed later. With these simplifications at NLO, there are in total 628 loop diagrams produced by the program MADGRAPH5_AMC@NLO [19], and 42 real emission diagrams by FEYNARTS [30] with quark, anti-quark, and photon initial states.

1. Renormalization

The calculation of one-loop diagrams has been performed in the t'Hooft-Feynman gauge with the program MADLOOP [31]. Several packages are linked by MADLOOP for the reduction of tensor integrals, each based on one of two distinct procedures: the Tensor Integral Reduction [32, 33] and the Ossola-Papadopoulos-Pittau method [34]. For simplicity, we neglect quark mixing and do not renormalize the quark mixing matrix.

The mass and field strength renormalization constants are determined within the on-shell renormalization scheme, except for the field strength Z_{AA} of the photon that is closely related to the renormalization of the electric charge. It can be obtained by imposing a renormalization condition at some momentum scale, or equivalently, by specifying the form of the renormalized fine structure constant. In this work we adopt two schemes. The G_μ scheme is defined by the choice [35]

$$\alpha_{G_\mu} = \frac{\sqrt{2}G_\mu M_W^2}{\pi} \left(1 - \frac{M_W^2}{M_Z^2}\right) \approx \frac{1}{132}, \quad (2)$$

where the Fermi constant G_μ is determined from the muon decay experiment, while the $\alpha(M_Z)$ scheme is obtained by evolving the physical fine structure constant $\alpha(0) \approx 1/137$ from zero momentum transfer to the scale M_Z , yielding $\alpha(M_Z) \approx 1/129$. The numerical value of α in both schemes differ from $\alpha(0)$, which is obtained by requiring that all high order corrections to the electron-photon 3-point function vanish in the Thomson limit [35, 36]. The differences are sensitive to the light fermion masses on which the loop contribution to the photon wave function depend. The sensitivity manifests as logarithmic terms of the form $\ln m_f$ [35, 37], indicating a collinear divergence in the on-shell photon wave function as the fermion masses m_f approach 0. It is straightforward to show that in the G_μ and $\alpha(M_Z)$ schemes, Z_{AA} , as well as the charge renormalization constant Z_e , are free from the collinear divergence, such that the definition of the physical charge on-shell is maintained. As long as no external photons are present in the LO process, we are able to consistently implement the renormalization constants and neglect the small mass m_f in the calculation of the loop diagrams with dimensional regularization.

2. Factorization

After factorizing the parton distribution functions (PDFs) of the incoming quarks, their mass can be safely set to zero in the partonic scattering amplitudes initiated by these flavors. The mass singularities from the initial state photon-quark splitting signal our ignorance of the nonperturbative interactions of the partons in the proton below some factorization scale μ_F , on which the QED evolution of the PDFs depends. The corresponding poles in the hard scattering process are subtracted by adding a collinear counter term to the squared amplitudes. In this calculation we use the PDF set CT14qed.inc-proton [38] from the LHAPDF library [39] with the NLO QED evolution. The collinear counter term is consistently implemented in the $\overline{\text{MS}}$ factorization scheme.

On the other hand, the incoming electron has no internal structure to accommodate for the singularity from collinear radiations. In principle, one could keep m_e throughout the calculation and retain the dependence of the hard scattering amplitude on $\ln m_e$. This collinear singularity is physical and would break the convergence of the perturbative calculation if m_e were too small. Fortunately, the size of the fine structure constant at the electro-weak scale ensures the convergence of the perturbation series in most of the kinematic regions we will consider (see Sec. III C). However, in reducing the tensor integrals we find that some of the pentagon diagrams are sensitive to the electron mass, which leads to a significant disagreement among different reduction programs when m_e takes a small but non-zero value. This numerical instability is cured if m_e is neglected and the mass singularity is regulated dimensionally.

With this observation, we factor out the mass singularity from the collinear photon radiation off the incoming electron. The singular terms are then put in a lepton distribution function, with the form to $\mathcal{O}(\alpha)$ in the $\overline{\text{MS}}$ factorization scheme given by [40] (Here and below, α can be α_{G_μ} or $\alpha(M_Z)$, depending on the renormalization scheme used)

$$f_e(x) = \delta(1-x) + \frac{\alpha}{2\pi} \left[\frac{1+x^2}{1-x} \ln \frac{\mu_F^2}{(1-x)^2 m_e^2} \right]_+. \quad (3)$$

This leaves a hard scattering part independent of the electron mass. Following this path, we are able to avoid the numerical problem during the reduction procedure and the calculation of the hard scattering cross section can be greatly simplified.

3. 4-particle final states

4-particle final states with an on-shell Higgs at the parton level can be produced at NLO ($\mathcal{O}(\alpha^4)$) via $e^- + q \rightarrow \nu_e + \gamma + q' + H$ and $e^- + \gamma \rightarrow \nu_e + q + q' + H$. Example diagrams for these processes are given in Fig. 4. There can be resonant W propagators,

as shown by the last diagram in the figure. To handle such cases, we employ the complex-mass scheme [41–43] in the calculation of the amplitudes.

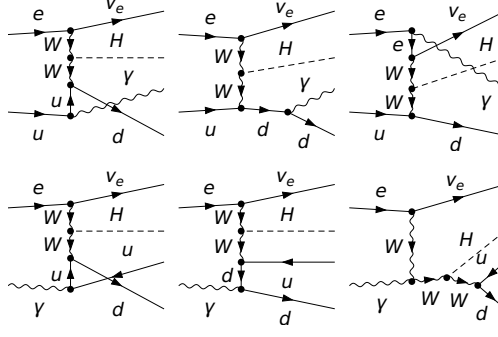


FIG. 4: Representative real-emission diagrams for CC WBF at the LHeC. The first and second lines correspond respectively to the processes $e^- + q \rightarrow \nu_e + \gamma + q' + H$ and $e^- + \gamma \rightarrow \nu_e + q + q' + H$, in which $q = u, q' = d$.

The subtraction procedure starts by constructing terms that asymptotically approach the squared amplitude for the real emission process in the phase space region where the radiated particle (the emittee) becomes soft or collinear to the emitter. The dipole structure of the subtraction term is encoded in the charge correlation between the splitting pair and a third particle (spectator). Three types of dipoles are present for our processes and the subtraction term takes the form [29]

$$|\mathcal{M}_{sub}|^2 = \sum_{i,j} \sum_a \mathcal{D}_{ij}^a + \sum_{a,j} \sum_{k \neq j} \mathcal{D}_{j,k}^a + \sum_{a,j} \sum_{b \neq a} \mathcal{D}_j^{a,b}. \quad (4)$$

The indices i, j, k denote the emitter, emittee, and spectator, respectively, in the final state. a and b are initial state partons, where a plays the role of the spectator in \mathcal{D}_{ij}^a , and the emitter in $\mathcal{D}_{j,k}^a$ and $\mathcal{D}_j^{a,b}$, while b is the spectator. Here we extend the meaning of “parton” to include the initial state electron and photon that undergo electromagnetic interactions. The outer sum is over all possible choices of the splitting pairs, while the inner sum runs over the spectators. The diagrammatic representation of the three dipole types can be found in Ref. [26, 29]. In each dipole term, the singular behavior is extracted and encoded in a splitting function factorized from the corresponding born process, whose final state coincides with the kinematics of the radiative process in the soft or collinear limit. To obtain the born kinematics one combines the emitter and emittee from the corresponding splitting process to a single particle. The momenta of this particle and of the spectator are then shifted in such a way as to respect momentum conservation and on-shell conditions for the 3-particle final state [26]. The explicit expressions for the dipole terms and shifted momenta are given in Appendix A

Now we subtract these terms from the real emission part to remove any singularity in the phase space. The cross section is thereby expressed by

$$\sigma_4^{NLO} = \sum_b \int_0^1 d\eta_b f_b(\eta_b, \mu_F) \frac{1}{2\hat{s}} d\Phi_4 \left\{ |\mathcal{M}_R^b|^2 F^{(2)}(p_1, p_2, p_3, p_4; P_A, p_b) - |\mathcal{M}_{sub}^b|^2 \right\}, \quad (5)$$

where b denotes the parton that collides with the electron; it can be a quark, anti-quark, or photon, and plays the role of either an emitter or spectator. It should not be confused with the “ b ” in Eq. 4, which only denotes a spectator.

In order to construct collinear-safe observables, we assign a jet function $F^{(2)}$ to the real emission process to combine quarks and photons according to a certain choice of the jet algorithm. $F^{(2)}$ depends on the momenta of the 4-particle final state. Correspondingly, for each dipole term in Eq. 4, there is a function $F^{(1)}$ of the 3-particle phase space obtained from the real emission process via the procedure described after Eq. 4. $F^{(1)}$ ’s are implicitly included in Eqs. 4 and 5, as well as in Eq. 1. To ensure the cancellation of singularities, $F^{(2)}$ must approach the corresponding $F^{(1)}$ in various soft and collinear limits.

At this order, only the delta function term of the electron PDF in Eq. 3 contributes, which is trivially integrated out in Eq. 5 over the electron momentum fraction (This is also true for the LO case in Eq. 1). Since the integrand in Eq. 5 is finite, integration over the 4-particle phase space can be safely done in four dimensions with numerical methods.

4. 3-particle final states

Evidently, the subtracted dipole terms are auxiliary and need to be put back to avoid any artifact in the calculation. The structure of these terms is simple enough such that the singularities can be isolated in a factorized form after an analytical

integration over a one-particle phase space. These “integrated” dipole terms have a phase space with one fewer particle, and are added back to combine with the loop diagrams. The result contains only collinear singularities from the initial state radiations, which are then canceled by the collinear counter terms from the factorization procedure.

The dipole and collinear counter terms can be reorganized into a term \mathbf{I} that contains all the soft and collinear divergences present in the loop diagrams, and two other terms \mathbf{K} and \mathbf{P} that have finite remainders after cancellation of singularities. In particular, \mathbf{K} and \mathbf{P} include the finite terms from factorization of initial state collinear singularities. The terms that depend on the choice of factorization scheme are contained in \mathbf{K} , while \mathbf{P} gives the dependence on the factorization scale μ_F . The cross section from the 3-particle final states can therefore be expressed in terms of the contribution from the born and loop processes together with \mathbf{I}, \mathbf{K} and \mathbf{P} [26, 28, 29]

$$\begin{aligned} \sigma_3^{NLO} = & \sum_b \int d\eta_b f_b(\eta_b, \mu_F) \left\{ \int \frac{1}{2\hat{s}} d\Phi_3^{(4)} \left[V_{ab}(\Phi_3, P_A, p_b) + B_{ab}(\Phi_3, P_A, p_b) \mathbf{I}^b(\epsilon, \mu^2) \right]_{\epsilon=0} \right. \\ & + \sum_{a'} \int dx_a \int \frac{1}{2\hat{s}} d\Phi_3^{(4)} B_{a'b}(\Phi_3^{(4)}, x_a P_A, p_b) \left[\mathbf{K}_{aa'}^b(x_a) + \mathbf{P}_{aa'}^b(x_a; \mu_F^2) \right] \\ & + \sum_{b'} \int dx_b \int \frac{1}{2\hat{s}} d\Phi_3^{(4)} B_{ab'}(\Phi_3^{(4)}, P_A, x_b p_b) \left[\mathbf{K}_{bb'}^a(x_b) + \mathbf{P}_{bb'}^a(x_b; \mu_F^2) \right] \Big\} \\ & + \sum_b \int d\eta_a d\eta_b f_e^{\mathcal{O}(\alpha)}(\eta_a, \mu_F) f_b(\eta_b, \mu_F) \int \frac{1}{2\hat{s}} d\Phi_3^{(4)} B_{ab}(\Phi_3^{(4)}, p_a, p_b). \end{aligned} \quad (6)$$

Here B is the squared born amplitude, and V the interference between born and loop processes. a labels the electron and b the parton from the proton; a' (b') is the flavor from the splitting of a (b) that enters the LO hard scattering amplitude. The beam and initial state parton momenta are related by $p_a = \eta_a P_A$ and $p_b = \eta_b P_B$. In the last line of Eq. 6, we use the $\mathcal{O}(\alpha)$ term of the electron PDF, as is indicated by its superscript. The first three lines are from convolution with the delta term in Eq. 3, for which $\eta_a = 1$. In each term on the R.H.S of Eq. 6, the phase space $\Phi_3^{(4)}$ and flux factor $1/2\hat{s}$ both depend on the CM energy of the corresponding born factor. The subscripts of B and V in the first and last lines show that the flavors entering these factors are the same as those from the incoming beams (i.e., from the PDFs). In contrast, the subscripts of \mathbf{K} and \mathbf{P} show that the flavors may change before and after initial state splittings in these terms. The superscript of \mathbf{K} or \mathbf{P} labels the other incoming particle that does not go through the splitting. As in Eqs. 1, 4 and 5, we implicitly include a jet function $F^{(1)}$ for the phase space of each term in Eq. 6.

The loop integrals in V are done in $d = 4 - 2\epsilon$ dimensions and all singularities after renormalization manifest as single and double poles, to be canceled exactly by the poles from \mathbf{I} . Therefore, the phase space Φ_3 of V and B in the first line of Eq. 6 should be the same, i.e., both in either 4 or d dimensions. After the poles are canceled, one takes the limit $\epsilon \rightarrow 0$ and performs the phase space integration in 4 dimensions, as denoted by “ $\epsilon = 0$ ” and “ $d\Phi_3^{(4)}$ ” in the first line. While \mathbf{I}, \mathbf{K} and \mathbf{P} all contribute to the quark/anti-quark induced processes, photon induced processes only receive contribution from non-singular terms \mathbf{K} and \mathbf{P} .

The expressions of \mathbf{I}, \mathbf{K} and \mathbf{P} for specific processes are listed in Appendix B. The integrand of all terms in Eq. 6 are finite and the phase space can be integrated over numerically in four dimensions. Once σ_3^{NLO} and σ_4^{NLO} are obtained, we combine them to give the full corrections to the cross section at NLO. Note that neither of the two contributions alone is physical because of the auxiliary dipole terms introduced.

III. Numerical result

A. Setup

To make numerical predictions for the WBF cross section, we take the energies of the incoming electron and proton to be

$$E_e = 140 \text{ GeV}, \quad E_p = 7 \text{ TeV}, \quad (7)$$

corresponding to a CM energy $\sqrt{s} = 2\sqrt{E_p E_e} \approx 1.98$ TeV, which is the choice in the study of H - b coupling at the LHeC [13]. The renormalization and factorization scales are set to M_W . In addition, we use the following set of parameters

$$\begin{aligned} G_\mu &= 1.16639 \times 10^{-5} \text{ GeV}^{-2}, & \alpha_{G_\mu} &= 1/132.5, & \alpha(M_Z) &= 1/128.93, \\ M_W &= 80.419 \text{ GeV}, & \Gamma_W &= 2.09291 \text{ GeV}, & M_Z &= 91.188 \text{ GeV}, \\ \Gamma_Z &= 2.49877 \text{ GeV}, & c_W^2 &= 1 - s_W^2 = \frac{M_W^2}{M_Z^2}, \\ m_e &= 0.510998928 \text{ MeV}, & M_H &= 125 \text{ GeV}. \end{aligned} \quad (8)$$

As discussed in Sec. II B 1 and II B 2, the dominant fermion mass effect is incorporated into the renormalized fine structure constant as well as the electron distribution. Hence we do not specify the values of fermion masses here, and set them to zero throughout the calculation of the hard scattering cross section. The only exception is the explicit use of m_e in the electron distribution from Eq. 3. As stated before, we use a unit CKM matrix in this work.

In this calculation, the tree level Feynman diagrams and amplitudes are produced and evaluated by the FEYNARTS, FORMCALC, and LOOPTOOLS package set [30, 44]. The analytical calculation of the dipole terms are carried out with the program *Mathematica*. The one-loop amplitudes are computed using the program MADLOOP [31] implemented by MADGRAPH5_AMC@NLO package [19]. We have developed our own code to generate the 3- and 4-particle phase space, over which the numerical integration is performed with the Vegas Monte-Carlo program implemented by the CUBA library [45].

B. Consistency checks

To verify the calculation we have done several checks at different levels. First, the tree-level amplitudes for born and real emission processes computed with FORMCALC are compared with those obtained from MADGRAPH5.

In the 4-particle final state part, we have made sure that the real emission contribution approach the corresponding dipole terms in various soft and collinear limits, and that the integrand after subtraction be stable in a Monte-Carlo integration. Also, the explicit form of the dipole terms for the real emission processes is compared numerically with the dipoles generated by MADDIPOLE [46, 47].

For the 3-particle final state terms, we have verified analytically in the case of triangle graphs that all double and single poles produced in dimensional regularization are canceled among the loop graphs (whose forms are derived from the scalar integrals in Ref. [37] after reduction), dipoles, and the collinear counter terms. This verification is then carried out for all loop diagrams (computed with MADLOOP) numerically. In the finite part, we checked that the dependence on the renormalization scale is canceled between the loop and dipole terms.² There is no running of the coupling and masses in the renormalization schemes we choose, and the cancellation of the scale dependence is exact at the order we are working with.

C. Phenomenology

First, we report the result of the integrated cross section computed in two renormalization schemes. Table. I lists contribution from LO and NLO terms, where all W fusion processes that produce a Higgs boson are included. There is a prominent difference

Schemes	total	LO	3-particle	4-particle
G_μ	223.27	245.48	-20.48	-1.73
α_{M_Z}	216.74	266.48	-47.82	-1.93

TABLE I: Integrated cross sections in fb for CC WBF at the LHeC at LO and NLO, computed in two renormalization schemes G_μ and α_{M_Z} . The electron and proton beam energies are 140 GeV and 7 TeV, respectively.

in the LO cross sections obtained in the two schemes. This is solely due to the difference in the renormalized fine structure constants. In the G_μ scheme, the NLO terms reduces the LO result by $\sim 9\%$, while the relative correction in the $\alpha(M_Z)$ scheme is as large as $\sim 18\%$. The sum of LO and NLO result, however, agree in both schemes, up to a difference at one higher order.

² Note that the factorization scale independence could not be checked in this calculation because the PDF sets undergo QCD evolution. The corresponding QCD corrections need to be included in order to cancel the scale dependence at the order of evolution.

This in fact provides another consistency check for the calculation. In both schemes the bulk of the NLO corrections come from the 3-particle final states. The allocation of the contribution between 3- and 4- particle final states is an artifact that relies on the choice of the subtraction terms away from the divergent region of the phase space. But this will of course not affect the sum of the two contributions. Notice that the coupling in the G_μ scheme is smaller and leads to a much faster convergence of the perturbation series. In the following discussion we shall stick with this scheme.

Next, we turn to the study of distributions. As remarked in the introduction, a distinctive feature of the WBF event in e - p collisions is an energetic jet produced in the far backward direction with large transverse momentum (we take the direction of the incoming electron to be forward). This is very prominent at the LHeC because the final state is strongly boosted along the direction of the proton. The decay product of the Higgs tends to be well separated from this jet, with a rapidity near the central region. To make full use of this event shape, we follow the strategy in Ref. [13, 17] and identify the “tagging jet” as the one with the largest transverse momentum, imposing the cuts

$$p_T^j > 30 \text{ GeV}, \quad -5 < \eta_j < -1, \quad M_{H,j} > 250 \text{ GeV}, \quad (9)$$

where p_T^j and η^j are the transverse momenta and rapidity of the tagging jet; $M_{H,j}$ is the invariant mass of the Higgs-tagging jet system. Further, the large momentum transfer to the neutrino from the hard scattering is reflected by the requirement

$$\cancel{E}_T > 25 \text{ GeV}, \quad (10)$$

with \cancel{E}_T denoting the transverse energy of the neutrino. Normally one also applies basic cuts on the Higgs decay products, which is apparently not done in our case as we are not performing a full signal-background analysis in this work.

In the following, we present distributions in various observables \mathcal{O} computed at LO and NLO (here “NLO” also includes the LO contribution). Each jet function in Eqs. 5 and 6 plays the role of constructing the observable with the momenta from its argument list.³ Here we use k_T algorithm [48–50] with the parameter $D = 0.8$ to define jet observables. In order to show the relative correction from the EW radiations with respect to the LO result, we define the K factor

$$K(\mathcal{O}) \equiv \frac{d\sigma^{NLO}/d\mathcal{O}}{d\sigma^{LO}/d\mathcal{O}}, \quad (11)$$

as a function of the observable \mathcal{O} .

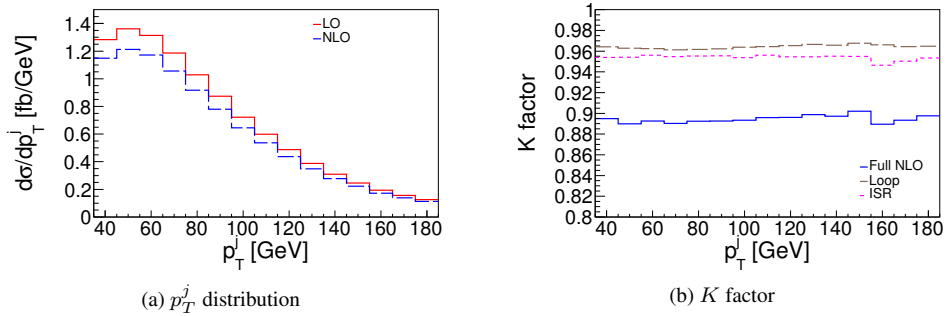


FIG. 5: Distribution in the transverse momentum p_T^j of the tagging jet (a), and the corresponding K factors (b).

We first display the differential distribution of the tagging jet transverse momentum p_T^j in Fig. 5 (a), where the LO and NLO curves are in red and blue respectively. The cross section peaks near small value of p_T^j and drops apace with increasing jet transverse momentum, with an average p_T^j of order the W boson mass. The relative EW correction is about -10% over the broad p_T^j range, as shown by the blue curve on the right. In addition, we show separately the K factor of the two dominant contributions at NLO. The short-dashed magenta line gives the correction from the initial state radiation (ISR) of the photon off the electron, which is about -5% and is consistent with the result obtained by Ref. [16]. This collinear radiation results in large logarithmic terms of the form $\sim \ln m_e$ (See the last line of Eq. 6), and gives the main part of the QED corrections. Another contribution in long-dashed brown is from the EW loop diagrams, with IR singular terms removed by subtractions. In Fig. 5 it is of the similar size as ISR, and both curves have a rather flat shape.

³ Note that the momenta for a dipole term are transformed from those of the corresponding real emission process.

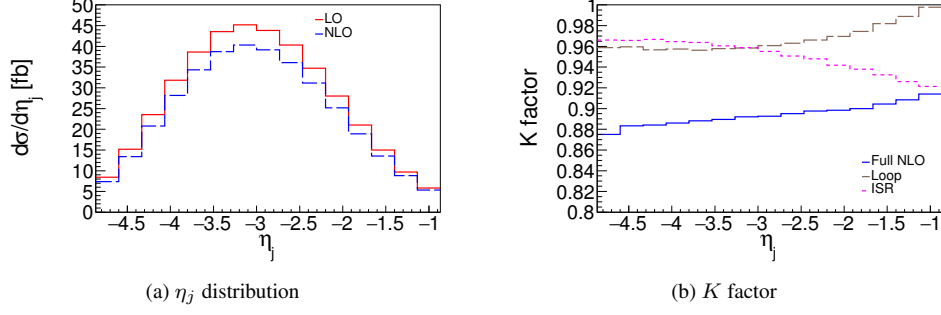


FIG. 6: Distribution in the rapidity η_j of the tagging jet (a), and the corresponding K factors (b).

The distribution in the rapidity η_j of the tagging parton is shown in Fig. 6, where the peak is clearly located in the backward region. The EW corrections vary between -8% and -12%, with a slow increase as η_j approaches the central region. The loop contribution increases more rapidly at large η_j than the full NLO curve, while the ISR terms display an opposite trend in this region.

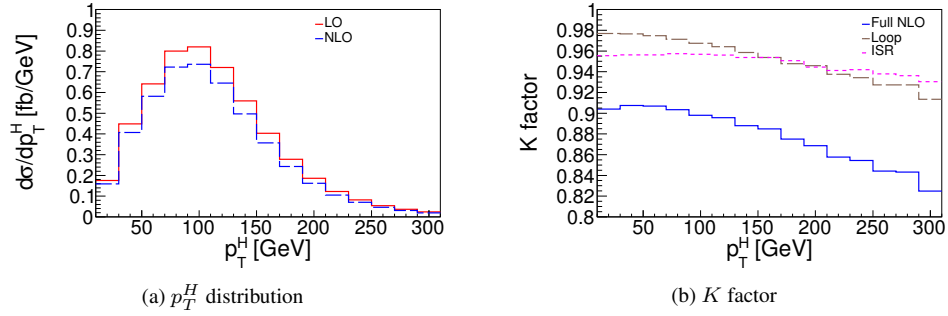


FIG. 7: Distribution in the transverse momentum p_T^H of the Higgs boson (a), and the corresponding K factors (b).

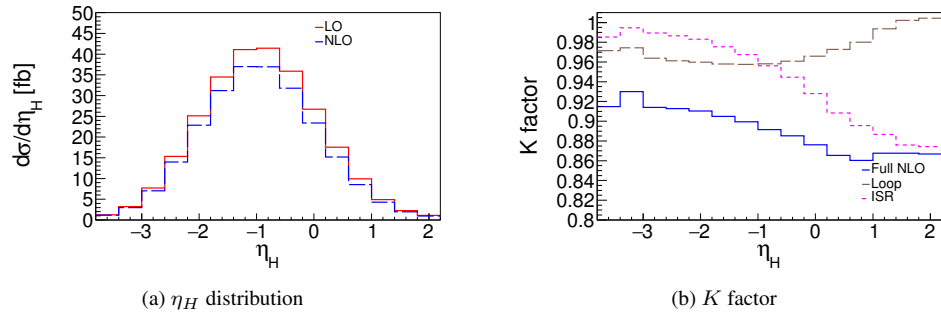


FIG. 8: Distribution in the rapidity η_H of the Higgs boson (a), and the corresponding K factors (b).

Figs. 7 and 8 show that the Higgs observables (transverse momentum p_T^H and rapidity η_H) are more sensitive to the NLO terms. The size of the corrections can be as large as -17% (for p_T^H) or -14% (for η_H). There are also considerable changes of the K factors in the ranges of both variables. In particular, ISR terms play a prominent role in the η_H distribution. It is argued [51, 52] that the ISR contribution can be enhanced near the threshold for producing the final state. This is already seen at large p_T^H or positive η_H in the plots. The analysis in Ref. [13] shows that the WBF process tends to produce the final state with a larger invariant mass than that of the background. This may induce a heavier suppression of the WBF signal from the ISR terms in the region where the signal dominates, potentially making the probe of e.g. H - b Yukawa more difficult. Of course, radiative corrections for the background need also be accounted for in order to yield a full phenomenological effect.

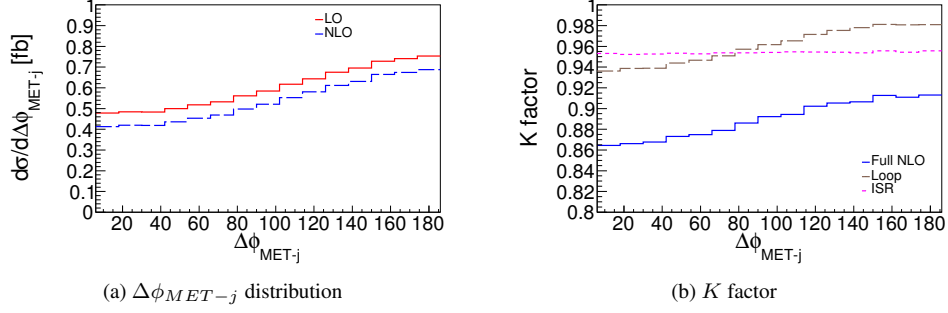


FIG. 9: Distribution in the azimuthal angle correlation between the tagging jet and the missing transverse energy (a), and the corresponding K factors (b).

Finally, we present in Fig. 9 the distribution in the azimuthal angle between the tagging jet and missing transverse energy. This distribution is sensitive to the anomalous HWW couplings [53, 54], whereas in the SM the differential cross section exhibits only a steady increase with the increasing $\Delta\phi_{MET-j}$. The relative EW corrections also display a mild dependence on $\Delta\phi_{MET-j}$ and change in the range between -14% to -7%. This shape distortion at NLO is caused by the loop contribution that is insensitive to the electron mass m_e . ISR in this case adds essentially a constant correction of -5%. At this point, it is still hard to predict the role of the loop terms in a systematic study of Higgs phenomenology at the LHeC.

IV. Conclusion

We have computed the NLO EW corrections for the Higgs production process via CC WBF at the LHeC. This is the first calculation that takes into account the full EW effect at one loop for this process. To handle the singularities of various origins in the amplitudes, we have worked in the dipole subtraction formalism and factorized the collinear radiation of the initial states. We have developed our own program to implement the subtraction procedure and carry out the numerical integration over the phase space. Checks at many levels have been done to verify the consistency of the calculation.

For the CM energy at 1.98 TeV, we have found a relative correction of 9% (18%) in the total cross section with no cuts using the G_μ (α_{M_Z}) renormalization scheme. The agreement between the two schemes are significantly improved when the LO and NLO-correction terms are added. The differential cross sections for several observables have also been computed in the G_μ scheme under the selection cuts for the WBF process. The corrections for these variables are within -20%. Sizable distortion of the distributions are also observed due to the ISR and loop corrections. Despite the smallness of the EW coupling α as compared with the strong coupling α_S , EW corrections are considerably larger than QCD corrections at NLO both because of the large number of diagrams (compared with the number of the QCD loop diagrams), and because of the ISR effect associated with photon radiations by the electron beam. The results show that the EW corrections is very important for the study of Higgs phenomenology at the LHeC and should not be neglected in a full analysis of the WBF process.

V. Acknowledgement

The authors thank Lilin Yang, Ruibo Li, and Xiang Lv for helpful discussions. B.W. would like to thank Zhuoni Qian for useful suggestions on histograming, and Ted Rogers for providing a very important reference. This work was supported by National Science Foundation of China (11875232, 12147103, 12105068). B.W. was also supported by Hangzhou Normal University Start-up Funds.

A. Expressions for the 4-particle final states

The specific form of the subtraction term for the quark- and anti-quark-initiated process

$$e^-(p_a) + q(p_b) \rightarrow \nu_e(p_1) + \gamma(p_2) + q'(p_3) + H(p_4)$$

reads

$$\begin{aligned}
|\mathcal{M}_{sub}|^2 &= \mathcal{D}_{q'\gamma}^e + \mathcal{D}_{\gamma q'}^e + \mathcal{D}_{\gamma}^{e,q} + \mathcal{D}_{q'\gamma}^q + \mathcal{D}_{\gamma q'}^q + \mathcal{D}_{\gamma}^{q,e} \\
&= -\frac{1}{2p_3p_2} \frac{1}{x_{32,a}} 8\pi\mu^{2\epsilon} \alpha \left[\frac{2}{2-x_{32,a}-z_{3a}} - 1 - z_{3a} - \epsilon(1-z_{3a}) \right] \mathcal{Q}_{3a}^2 |\mathcal{M}_0^q(x_{32,a}p_a + P_{3a}; x_{32,a}p_a)|^2 \\
&\quad - \frac{1}{2p_ap_2} \frac{1}{x_{a2,3}} 8\pi\mu^{2\epsilon} \alpha \left[\frac{2}{2-x_{a2,3}-z_{3a}} - 1 - x_{a2,3} - \epsilon(1-x_{a2,3}) \right] \mathcal{Q}_{a3}^2 |\mathcal{M}_0^q(x_{a2,3}p_a + P_{3a}; x_{a2,3}p_a)|^2 \\
&\quad - \frac{1}{2p_ap_2} \frac{1}{x_{a2,b}} 8\pi\mu^{2\epsilon} \alpha \left[\frac{2}{1-x_{a2,b}} - 1 - x_{a2,b} - \epsilon(1-x_{a2,b}) \right] \mathcal{Q}_{ab}^2 |\mathcal{M}_0^q(\tilde{p}_i(x_{a2,b}); x_{a2,b}p_a)|^2 \\
&\quad - \frac{1}{2p_3p_2} \frac{1}{x_{32,b}} 8\pi\mu^{2\epsilon} \alpha \left[\frac{2}{2-x_{32,b}-z_{3b}} - 1 - z_{3b} - \epsilon(1-z_{3b}) \right] \mathcal{Q}_{3b}^2 |\mathcal{M}_0^q(x_{32,b}p_b + P_{3b}; x_{32,b}p_b)|^2 \\
&\quad - \frac{1}{2p_bp_2} \frac{1}{x_{b2,3}} 8\pi\mu^{2\epsilon} \alpha \left[\frac{2}{2-x_{b2,3}-z_{3b}} - 1 - x_{b2,3} - \epsilon(1-x_{b2,3}) \right] \mathcal{Q}_{b3}^2 |\mathcal{M}_0^q(x_{b2,3}p_b + P_{3b}; x_{b2,3}p_b)|^2 \\
&\quad - \frac{1}{2p_bp_2} \frac{1}{x_{b2,a}} 8\pi\mu^{2\epsilon} \alpha \left[\frac{2}{1-x_{b2,a}} - 1 - x_{b2,a} - \epsilon(1-x_{b2,a}) \right] \mathcal{Q}_{ba}^2 |\mathcal{M}_0^q(\tilde{p}_i(x_{b2,a}); x_{b2,a}p_b)|^2,
\end{aligned} \tag{A1}$$

where \mathcal{M}_0^q is the amplitude for the born process $eq \rightarrow \nu_e q' H$. The momentum fractions are defined as

$$\begin{aligned}
x_{32,a} &= x_{a2,3} = 1 - \frac{p_3p_2}{(p_3+p_2)p_a}, & z_{3a} &= \frac{p_3p_a}{(p_3+p_2)p_a}, \\
x_{32,b} &= x_{b2,3} = 1 - \frac{p_3p_2}{(p_3+p_2)p_b}, & z_{3b} &= \frac{p_3p_b}{(p_3+p_2)p_b}, \\
x_{a2,b} &= x_{b2,a} = 1 - \frac{p_2(p_a+p_b)}{p_ap_b}.
\end{aligned} \tag{A2}$$

As remarked in Sec. IIB 3, the born amplitudes in Eqs. A1 depend on the shifted momenta obtained from the corresponding radiative processes. These momenta are shown as the arguments of the born amplitudes, where the momenta from the initial/final state is on the right/left of the semicolon (Momenta with no modifications are not shown). They are related to the momenta of the real emission processes by

$$\begin{aligned}
P_{3a} &= p_3 + p_2 - p_a = p_3 + p_2 - (1 - x_{32,a})p_a - x_{32,a}p_a, \\
P_{3b} &= p_3 + p_2 - p_b = p_3 + p_2 - (1 - x_{32,b})p_b - x_{32,b}p_b, \\
P_{ab} &= p_a + p_b - p_2, & \tilde{P}_{ab} &= x_{a2,b}p_a + p_b, \\
\tilde{p}_i^\mu &= \Lambda_\nu^\mu p_i^\nu = \left(g_\nu^\mu - \frac{(P_{ab} + \tilde{P}_{ab})^\mu (P_{ab} + \tilde{P}_{ab})_\nu}{P_{ab}^2 + P_{ab}\tilde{P}_{ab}} + \frac{\tilde{P}_{ab}^\mu P_{ab,\nu}}{P_{ab}^2} \right) p_i^\nu.
\end{aligned} \tag{A3}$$

Note that \tilde{p}_i for all final state particles in $\mathcal{D}_{\gamma}^{e,q}$ and $\mathcal{D}_{\gamma}^{q,e}$ must transform according to Eq. A3. The charge correlator \mathcal{Q}_{ik}^2 is defined by the charges of the flavor i and k as

$$\mathcal{Q}_{ik}^2 = Q_i Q_k \theta_i \theta_k, \tag{A4}$$

where $\theta_{i/k}$ is 1 (−1) if it is in the final (initial) state. For quark-initiated processes in our calculation, i.e., $q = u, c$, and $q' = d, s$, the charge correlators in Eq. A1 are

$$\begin{aligned}
\mathcal{Q}_{3a}^2 &= \mathcal{Q}_{a3}^2 = Q_3(-Q_a) = -\frac{1}{3}, & \mathcal{Q}_{3b}^2 &= \mathcal{Q}_{b3}^2 = Q_3(-Q_b) = \frac{2}{9}, \\
\mathcal{Q}_{ab}^2 &= \mathcal{Q}_{ba}^2 = (-Q_a)(-Q_b) = -\frac{2}{3},
\end{aligned} \tag{A5}$$

where each initial state fermion acquires a minus sign on its charge. The anti-quark-initiated processes, with $q = \bar{d}, \bar{s}$, and $q' = \bar{u}, \bar{c}$, differ from the corresponding quark-initiated processes only by the charge correlators, which are

$$\mathcal{Q}_{3a}^2 = \mathcal{Q}_{a3}^2 = -\frac{2}{3}, \quad \mathcal{Q}_{3b}^2 = \mathcal{Q}_{b3}^2 = \frac{2}{9}, \quad \mathcal{Q}_{ab}^2 = \mathcal{Q}_{ba}^2 = -\frac{1}{3}. \tag{A6}$$

For the photon-induced processes

$$e^-(p_a) + \gamma(p_b) \rightarrow \nu_e(p_1) + q(p_2) + q'(p_3) + H(p_4)$$

the subtraction term takes the form

$$\begin{aligned}
|\mathcal{M}_{sub}|^2 &= \mathcal{D}_{q,q'}^\gamma + \mathcal{D}_q^{\gamma,e} + \mathcal{D}_{q',q}^\gamma + \mathcal{D}_{q'}^{\gamma,e} \\
&= -\frac{1}{2p_b p_2} \frac{1}{x_{b2,3}} 8\pi\mu^{2\epsilon} \alpha \left[1 - \epsilon - 2x_{b2,3}(1 - x_{b2,3}) \right] N_{C,f} \mathcal{Q}_{b23}^2 |\mathcal{M}_0^\gamma(x_{b2,3}p_b + P_{3b}, x_{b2,3}p_b)|^2 \\
&\quad - \frac{1}{2p_b p_2} \frac{1}{x_{b2,a}} 8\pi\mu^{2\epsilon} \alpha \left[1 - \epsilon - 2x_{b2,a}(1 - x_{b2,a}) \right] N_{C,f} \mathcal{Q}_{b2a}^2 |\mathcal{M}_0^\gamma(\tilde{p}_i, x_{b2,a}p_b)|^2 \\
&\quad - \frac{1}{2p_b p_3} \frac{1}{x_{b3,2}} 8\pi\mu^{2\epsilon} \alpha \left[1 - \epsilon - 2x_{b3,2}(1 - x_{b3,2}) \right] N_{C,f} \mathcal{Q}_{b32}^2 |\mathcal{M}_0^\gamma(x_{b3,2}p_b + P_{3b}, x_{b3,2}p_b)|^2 \\
&\quad - \frac{1}{2p_b p_3} \frac{1}{x_{b3,a}} 8\pi\mu^{2\epsilon} \alpha \left[1 - \epsilon - 2x_{b3,a}(1 - x_{b3,a}) \right] N_{C,f} \mathcal{Q}_{b3a}^2 |\mathcal{M}_0^\gamma(\tilde{p}_i, x_{b3,a}p_b)|^2,
\end{aligned} \tag{A7}$$

where \mathcal{M}_0^γ is the amplitude for the born process $e\bar{q} \rightarrow \nu_e q' H$ (or equivalently, $e\bar{q}' \rightarrow \nu_e q H$). In addition to the definitions made in Eq. A2, we have

$$x_{b3,2} = 1 - \frac{p_3 p_2}{(p_3 + p_2)p_b}, \quad x_{b3,a} = 1 - \frac{p_3(p_a + p_b)}{p_a p_b}, \quad N_{C,f} = 3. \tag{A8}$$

The “tilde” symbol in the subscript of each charge correlator denotes the flavor from the photon splitting that enters the corresponding born process, namely, $\tilde{b}2$ denotes \bar{q} and $\tilde{b}3$ denotes \bar{q}' . The charge correlators for $q = \bar{u}, \bar{c}$, and $q' = d, s$ are

$$\mathcal{Q}_{b23}^2 = \frac{2}{9}, \quad \mathcal{Q}_{b32}^2 = \frac{2}{9}, \quad \mathcal{Q}_{b2a}^2 = -\frac{2}{3}, \quad \mathcal{Q}_{b3a}^2 = -\frac{1}{3}. \tag{A9}$$

B. Expressions for the 3-particle final states

In this appendix we list the specific form of the \mathbf{I}, \mathbf{K} and \mathbf{P} terms that are factorized from the born process

$$e^- + q \rightarrow \nu_e(p_1) + q'(p_2) + H(p_3),$$

where the momenta of the initial particles are not shown explicitly. For the corresponding \mathbf{I}, \mathbf{K} and \mathbf{P} terms, they are given by the arguments of the born factors in the first three lines of Eq. 6. Recall that there $p_a = P_A$, and $p_b = \eta_b P_B$.

The generic expressions for the quark- and anti-quark-initiated processes are

$$\begin{aligned}
\mathbf{I}^q(\epsilon) &= -\frac{\alpha}{2\pi} \frac{(4\pi)^\epsilon}{\Gamma(1-\epsilon)} \left[\frac{1}{\epsilon^2} + \frac{3}{2\epsilon} + 5 - \frac{\pi^2}{2} \right] \left\{ \mathcal{Q}_{2a}^2 \left(\frac{\mu^2}{2p_2 p_a} \right)^\epsilon + \mathcal{Q}_{a2}^2 \left(\frac{\mu^2}{2p_a p_2} \right)^\epsilon \right. \\
&\quad \left. + \mathcal{Q}_{ab}^2 \left(\frac{\mu^2}{2p_a p_b} \right)^\epsilon + \mathcal{Q}_{2b}^2 \left(\frac{\mu^2}{2p_2 p_b} \right)^\epsilon + \mathcal{Q}_{b2}^2 \left(\frac{\mu^2}{2p_b p_2} \right)^\epsilon + \mathcal{Q}_{ba}^2 \left(\frac{\mu^2}{2p_b p_a} \right)^\epsilon \right\},
\end{aligned} \tag{B1}$$

$$\begin{aligned}
\mathbf{K}_{ff'}^{c'}(x) &= \frac{\alpha}{2\pi} \left\{ -Q_f^2(1+x) \log \frac{1-x}{x} + Q_f^2(1-x) + \left[Q_f^2 \left(\frac{2}{1-x} \log \frac{1-x}{x} \right)_+ - \delta(1-x) \left((5-\pi^2) Q_f^2 \right) \right] \right. \\
&\quad \left. + \frac{3}{2} \frac{Q_{2f}^2}{Q_f^2} \left[\left(\frac{1}{1-x} \right)_+ + \delta(1-x) \right] - Q_{f'c'}^2 \left[-(1+x) \log(1-x) + \left[2 \left(\frac{\log(1-x)}{1-x} \right)_+ - \frac{\pi^2}{3} \delta(1-x) \right] \right] \right\},
\end{aligned} \tag{B2}$$

$$\mathbf{P}_{ff'}^{c'}(x, \mu_F^2) = \frac{\alpha}{2\pi} \left\{ -(1+x) + 2 \left(\frac{1}{1-x} \right)_+ + \frac{3}{2} \delta(1-x) \right\} \left[Q_{f2}^2 \log \frac{\mu_F^2}{2x p_f p_2} + Q_{f'c'}^2 \log \frac{\mu_F^2}{2x p_f p_{c'}} \right], \tag{B3}$$

where “ q ” in \mathbf{I}^q can be a quark or anti-quark. In $\mathbf{K}_{ff'}^b$ and $\mathbf{P}_{ff'}^b$, “ f ” can be a quark, anti-quark, or electron, while “ c' ” is the initial flavor not going through splitting (“ c ” without prime is reserved for the charm quark, which is only a particular case of c' . See below). Inserting the charge correlators for specific flavors, we find

$$\mathbf{I}^{u/c}(\epsilon) = -\frac{\alpha}{2\pi} \frac{(4\pi\mu^2)^\epsilon}{\Gamma(1-\epsilon)} \left[\frac{1}{\epsilon^2} + \frac{3}{2\epsilon} + 5 - \frac{\pi^2}{2} \right] \left\{ -\frac{2}{3} \left(\frac{1}{2p_a p_2} \right)^\epsilon - \frac{4}{3} \left(\frac{1}{2p_a p_b} \right)^\epsilon + \frac{4}{9} \left(\frac{1}{2p_b p_2} \right)^\epsilon \right\}, \tag{B4}$$

$$\mathbf{I}^{\bar{d}/\bar{s}}(\epsilon) = -\frac{\alpha}{2\pi} \frac{(4\pi\mu^2)^\epsilon}{\Gamma(1-\epsilon)} \left[\frac{1}{\epsilon^2} + \frac{3}{2\epsilon} + 5 - \frac{\pi^2}{2} \right] \left\{ -\frac{4}{3} \left(\frac{1}{2p_a p_2} \right)^\epsilon - \frac{2}{3} \left(\frac{1}{2p_a p_b} \right)^\epsilon + \frac{4}{9} \left(\frac{1}{2p_b p_2} \right)^\epsilon \right\}, \quad (\text{B5})$$

$$\mathbf{K}_{ee}^{u/c}(x) = \frac{\alpha}{2\pi} \left\{ -(1+x) \log \frac{1-x}{x} + (1-x) + \left(\frac{2}{1-x} \log \frac{1-x}{x} \right)_+ - \frac{9}{2} \left(\frac{1}{1-x} \right)_+ - \frac{2}{3} (1+x) \log(1-x) \right. \\ \left. + \frac{4}{3} \left(\frac{\log(1-x)}{1-x} \right)_+ + \left(\frac{7}{9} \pi^2 - \frac{19}{2} \right) \delta(1-x) \right\}, \quad (\text{B6})$$

$$\mathbf{K}_{uu/cc}^e(x) = \frac{\alpha}{2\pi} \left\{ -\frac{4}{9} (1+x) \log \frac{1-x}{x} + \frac{4}{9} (1-x) + \frac{4}{9} \left(\frac{2}{1-x} \log \frac{1-x}{x} \right)_+ + 3 \left(\frac{1}{1-x} \right)_+ - \frac{2}{3} (1+x) \log(1-x) \right. \\ \left. + \frac{4}{3} \left(\frac{\log(1-x)}{1-x} \right)_+ + \left(\frac{2}{9} \pi^2 + \frac{7}{9} \right) \delta(1-x) \right\}, \quad (\text{B7})$$

$$\mathbf{K}_{ee}^{\bar{d}/\bar{s}}(x) = \frac{\alpha}{2\pi} \left\{ -(1+x) \log \frac{1-x}{x} + (1-x) + \left(\frac{2}{1-x} \log \frac{1-x}{x} \right)_+ - \frac{9}{4} \left(\frac{1}{1-x} \right)_+ - \frac{1}{3} (1+x) \log(1-x) \right. \\ \left. + \frac{2}{3} \left(\frac{\log(1-x)}{1-x} \right)_+ + \left(\frac{8}{9} \pi^2 - \frac{29}{4} \right) \delta(1-x) \right\}, \quad (\text{B8})$$

$$\mathbf{K}_{dd/\bar{s}\bar{s}}^e(x) = \frac{\alpha}{2\pi} \left\{ -\frac{1}{9} (1+x) \log \frac{1-x}{x} + \frac{1}{9} (1-x) + \frac{1}{9} \left(\frac{2}{1-x} \log \frac{1-x}{x} \right)_+ + \frac{3}{4} \left(\frac{1}{1-x} \right)_+ - \frac{1}{3} (1+x) \log(1-x) \right. \\ \left. + \frac{2}{3} \left(\frac{\log(1-x)}{1-x} \right)_+ + \frac{7}{36} \delta(1-x) \right\}, \quad (\text{B9})$$

$$\mathbf{P}_{ee}^{u/c}(x, \mu_F^2) = \frac{\alpha}{2\pi} \left\{ -(1+x) + 2 \left(\frac{1}{1-x} \right)_+ + \frac{3}{2} \delta(1-x) \right\} \left[-\frac{1}{3} \log \frac{\mu_F^2}{2x p_a p_2} - \frac{2}{3} \log \frac{\mu_F^2}{2x p_a p_b} \right], \quad (\text{B10})$$

$$\mathbf{P}_{uu/cc}^e(x, \mu_F^2) = \frac{\alpha}{2\pi} \left\{ -(1+x) + 2 \left(\frac{1}{1-x} \right)_+ + \frac{3}{2} \delta(1-x) \right\} \left[\frac{2}{9} \log \frac{\mu_F^2}{2x p_b p_2} - \frac{2}{3} \log \frac{\mu_F^2}{2x p_a p_b} \right], \quad (\text{B11})$$

$$\mathbf{P}_{ee}^{\bar{d}/\bar{s}}(x, \mu_F^2) = \frac{\alpha}{2\pi} \left\{ -(1+x) + 2 \left(\frac{1}{1-x} \right)_+ + \frac{3}{2} \delta(1-x) \right\} \left[-\frac{2}{3} \log \frac{\mu_F^2}{2x p_a p_2} - \frac{1}{3} \log \frac{\mu_F^2}{2x p_a p_b} \right], \quad (\text{B12})$$

$$\mathbf{P}_{dd/\bar{s}\bar{s}}^e(x, \mu_F^2) = \frac{\alpha}{2\pi} \left\{ -(1+x) + 2 \left(\frac{1}{1-x} \right)_+ + \frac{3}{2} \delta(1-x) \right\} \left[\frac{2}{9} \log \frac{\mu_F^2}{2x p_b p_2} - \frac{1}{3} \log \frac{\mu_F^2}{2x p_a p_b} \right]. \quad (\text{B13})$$

For the photon-initiated processes, \mathbf{I} terms do not contribute. Also the electron splitting terms are of higher order in α and do not contribute in this case either. \mathbf{K} and \mathbf{P} terms take the form

$$\mathbf{K}_{\gamma f}^a(x) = \frac{\alpha}{2\pi} \left\{ N_{C,f} Q_f^2 \frac{1+(1-x)^2}{x} \log \frac{1-x}{x} + N_{C,f} Q_f^2 x(1-x) - Q_{fa}^2 N_{C,f} \frac{1+(1-x)^2}{x} \log(1-x) \right\}, \quad (\text{B14})$$

$$\mathbf{P}_{\gamma f}^a(x, \mu_F^2) = \frac{\alpha}{2\pi} \left\{ N_{C,f} \frac{1+(1-x)^2}{x} \right\} \left[Q_{f2}^2 \log \frac{\mu_F^2}{2x p_b p_2} + Q_{fa}^2 \log \frac{\mu_F^2}{2x p_a p_b} \right]. \quad (\text{B15})$$

The expressions for specific splitting processes are

$$\mathbf{K}_{\gamma u/c}^e(x) = \frac{\alpha}{2\pi} \left\{ \frac{4}{3} \frac{1+(1-x)^2}{x} \log \frac{1-x}{x} + \frac{4}{3} x(1-x) + 2 \frac{1+(1-x)^2}{x} \log(1-x) \right\}, \quad (\text{B16})$$

$$K_{\gamma\bar{d}/\bar{s}}^e(x) = \frac{\alpha}{2\pi} \left\{ \frac{1}{3} \frac{1+(1-x)^2}{x} \log \frac{1-x}{x} + \frac{1}{3} x(1-x) + \frac{1+(1-x)^2}{x} \log(1-x) \right\}, \quad (\text{B17})$$

$$P_{\gamma u/c}^e(x, \mu_F^2) = \frac{\alpha}{2\pi} \left\{ \frac{4}{3} \frac{1+(1-x)^2}{x} \right\} \left[\frac{1}{2} \log \frac{\mu_F^2}{2xp_b p_2} - \frac{3}{2} \log \frac{\mu_F^2}{2xp_a p_b} \right], \quad (\text{B18})$$

$$P_{\gamma\bar{d}/\bar{s}}^e(x, \mu_F^2) = \frac{\alpha}{2\pi} \left\{ \frac{1}{3} \frac{1+(1-x)^2}{x} \right\} \left[2 \log \frac{\mu_F^2}{2xp_b p_2} - 3 \log \frac{\mu_F^2}{2xp_a p_b} \right]. \quad (\text{B19})$$

-
- [1] ATLAS, G. Aad *et al.*, “Observation of a new particle in the search for the Standard Model Higgs boson with the ATLAS detector at the LHC,” *Phys. Lett. B* **716** (2012) 1–29, arXiv:1207.7214 [hep-ex].
- [2] CMS, S. Chatrchyan *et al.*, “Observation of a new boson at a mass of 125 GeV with the CMS experiment at the LHC,” *Phys. Lett. B* **716** (2012) 30–61, arXiv:1207.7235 [hep-ex].
- [3] ATLAS, CMS, L. Cadamuro, “Higgs boson couplings and properties,” *PoS LHCP2019* (2019) 101
- [4] ATLAS, CMS, J. M. Langford, “Combination of Higgs measurements from ATLAS and CMS : couplings and \parallel - framework,” *PoS LHCP2020* (2021) 136
- [5] ATLAS, CMS, S. Ordek, “Measurements of Higgs couplings to fermions and bosons at the LHC,” *PoS PANIC2021* (2022) 418
- [6] ATLAS, “A combination of measurements of Higgs boson production and decay using up to 139 fb⁻¹ of proton–proton collision data at $\sqrt{s} = 13$ TeV collected with the ATLAS experiment,”
- [7] CMS, “Combined Higgs boson production and decay measurements with up to 137 fb⁻¹ of proton-proton collision data at $\sqrt{s} = 13$ TeV,”
- [8] CMS, A. M. Sirunyan *et al.*, “Observation of the Higgs boson decay to a pair of τ leptons with the CMS detector,” *Phys. Lett. B* **779** (2018) 283–316, arXiv:1708.00373 [hep-ex]
- [9] ATLAS, M. Aaboud *et al.*, “Cross-section measurements of the Higgs boson decaying into a pair of τ -leptons in proton-proton collisions at $\sqrt{s} = 13$ TeV with the ATLAS detector,” *Phys. Rev. D* **99** (2019) 072001, arXiv:1811.08856 [hep-ex]
- [10] CMS, V. Khachatryan *et al.*, “Search for the standard model Higgs boson produced through vector boson fusion and decaying to $b\bar{b}$,” *Phys. Rev. D* **92** 3, (2015) 032008, arXiv:1506.01010 [hep-ex]
- [11] ATLAS, M. Aaboud *et al.*, “Search for the Standard Model Higgs boson produced by vector-boson fusion and decaying to bottom quarks in $\sqrt{s} = 8$ TeV pp collisions with the ATLAS detector,” *JHEP* **11** (2016) 112, arXiv:1606.02181 [hep-ex]
- [12] LHeC Study Group, J. L. Abelleira Fernandez *et al.*, “A Large Hadron Electron Collider at CERN: Report on the Physics and Design Concepts for Machine and Detector,” *J. Phys. G* **39** (2012) 075001, arXiv:1206.2913 [physics.acc-ph]
- [13] T. Han and B. Mellado, “Higgs Boson Searches and the H b anti- b Coupling at the LHeC,” *Phys. Rev. D* **82** (2010) 016009, arXiv:0909.2460 [hep-ph].
- [14] LHeC, FCC-he Study Group, P. Agostini *et al.*, “The Large Hadron-Electron Collider at the HL-LHC,” *J. Phys. G* **48** 11, (2021) 110501, arXiv:2007.14491 [hep-ex]
- [15] R. Li, B.-W. Wang, K. Wang, X. Zhang, and Z. Zhou, “Probing the charm Yukawa coupling at future e^-p and e^+e^- colliders,” *Phys. Rev. D* **100** 5, (2019) 053008, arXiv:1905.09457 [hep-ph]
- [16] J. Blumlein, G. J. van Oldenborgh, and R. Ruckl, “QCD and QED corrections to Higgs boson production in charged current $e p$ scattering,” *Nucl. Phys. B* **395** (1993) 35–59, arXiv:hep-ph/9209219
- [17] B. Jager, “Next-to-leading order QCD corrections to Higgs production at a future lepton-proton collider,” *Phys. Rev. D* **81** (2010) 054018, arXiv:1001.3789 [hep-ph]
- [18] R. Li, X.-M. Shen, B.-W. Wang, K. Wang, and G. Zhu, “Probing the trilinear Higgs boson self-coupling via single Higgs production at the LHeC,” *Phys. Rev. D* **101** 7, (2020) 075036, arXiv:1910.09424 [hep-ph]
- [19] J. Alwall, R. Frederix, S. Frixione, V. Hirschi, F. Maltoni, O. Mattelaer, H. S. Shao, T. Stelzer, P. Torrielli, and M. Zaro, “The automated computation of tree-level and next-to-leading order differential cross sections, and their matching to parton shower simulations,” *JHEP* **07** (2014) 079, arXiv:1405.0301 [hep-ph]
- [20] F. Buccioni, J.-N. Lang, J. M. Lindert, P. Maierhöfer, S. Pozzorini, H. Zhang, and M. F. Zoller, “OpenLoops 2,” *Eur. Phys. J. C* **79** 10, (2019) 866, arXiv:1907.13071 [hep-ph]
- [21] Sherpa, E. Bothmann *et al.*, “Event Generation with Sherpa 2.2,” *SciPost Phys.* **7** 3, (2019) 034, arXiv:1905.09127 [hep-ph]
- [22] J. Bellm *et al.*, “Herwig 7.0/Herwig++ 3.0 release note,” *Eur. Phys. J. C* **76** 4, (2016) 196, arXiv:1512.01178 [hep-ph]
- [23] S. Alioli, P. Nason, C. Oleari, and E. Re, “A general framework for implementing NLO calculations in shower Monte Carlo programs: the POWHEG BOX,” *JHEP* **06** (2010) 043, arXiv:1002.2581 [hep-ph]
- [24] S. Alioli, C. W. Bauer, C. J. Berggren, A. Hornig, F. J. Tackmann, C. K. Vermilion, J. R. Walsh, and S. Zuberi, “Combining Higher-Order Resummation with Multiple NLO Calculations and Parton Showers in GENEVA,” *JHEP* **09** (2013) 120, arXiv:1211.7049 [hep-ph]
- [25] W. Kilian, T. Ohl, and J. Reuter, “WHIZARD: Simulating Multi-Particle Processes at LHC and ILC,” *Eur. Phys. J. C* **71** (2011) 1742, arXiv:0708.4233 [hep-ph]
- [26] S. Catani and M. H. Seymour, “A General algorithm for calculating jet cross-sections in NLO QCD,” *Nucl. Phys. B* **485** (1997) 291–419, arXiv:hep-ph/9605323. [Erratum: Nucl.Phys.B 510, 503–504 (1998)]

- [27] S. Dittmaier, “A General approach to photon radiation off fermions,” *Nucl. Phys. B* **565** (2000) 69–122, arXiv:hep-ph/9904440
- [28] S. Catani, S. Dittmaier, M. H. Seymour, and Z. Trocsanyi, “The Dipole formalism for next-to-leading order QCD calculations with massive partons,” *Nucl. Phys. B* **627** (2002) 189–265, arXiv:hep-ph/0201036
- [29] M. Schönherr, “An automated subtraction of NLO EW infrared divergences,” *Eur. Phys. J. C* **78** 2, (2018) 119, arXiv:1712.07975 [hep-ph]
- [30] T. Hahn, “Generating Feynman diagrams and amplitudes with FeynArts 3,” *Comput. Phys. Commun.* **140** (2001) 418–431, arXiv:hep-ph/0012260
- [31] V. Hirschi, R. Frederix, S. Frixione, M. V. Garzelli, F. Maltoni, and R. Pittau, “Automation of one-loop QCD corrections,” *JHEP* **05** (2011) 044, arXiv:1103.0621 [hep-ph]
- [32] G. Passarino and M. J. G. Veltman, “One Loop Corrections for e^+e^- Annihilation Into $\mu^+\mu^-$ in the Weinberg Model,” *Nucl. Phys. B* **160** (1979) 151–207
- [33] A. I. Davydychev, “A Simple formula for reducing Feynman diagrams to scalar integrals,” *Phys. Lett. B* **263** (1991) 107–111
- [34] G. Ossola, C. G. Papadopoulos, and R. Pittau, “Reducing full one-loop amplitudes to scalar integrals at the integrand level,” *Nucl. Phys. B* **763** (2007) 147–169, arXiv:hep-ph/0609007
- [35] A. Denner and S. Dittmaier, “Electroweak Radiative Corrections for Collider Physics,” *Phys. Rept.* **864** (2020) 1–163, arXiv:1912.06823 [hep-ph]
- [36] A. Denner, “Techniques for calculation of electroweak radiative corrections at the one loop level and results for W physics at LEP-200,” *Fortsch. Phys.* **41** (1993) 307–420, arXiv:0709.1075 [hep-ph]
- [37] R. K. Ellis and G. Zanderighi, “Scalar one-loop integrals for QCD,” *JHEP* **02** (2008) 002, arXiv:0712.1851 [hep-ph]
- [38] C. Schmidt, J. Pumplin, D. Stump, and C. P. Yuan, “CT14QED parton distribution functions from isolated photon production in deep inelastic scattering,” *Phys. Rev. D* **93** 11, (2016) 114015, arXiv:1509.02905 [hep-ph].
- [39] A. Buckley, J. Ferrando, S. Lloyd, K. Nordström, B. Page, M. Rüfenacht, M. Schönherr, and G. Watt, “LHAPDF6: parton density access in the LHC precision era,” *Eur. Phys. J. C* **75** (2015) 132, arXiv:1412.7420 [hep-ph].
- [40] T. Liu, W. Melnitchouk, J.-W. Qiu, and N. Sato, “A new approach to semi-inclusive deep-inelastic scattering with QED and QCD factorization,” *JHEP* **11** (2021) 157, arXiv:2108.13371 [hep-ph]
- [41] A. Denner, S. Dittmaier, M. Roth, and D. Wackeroth, “Predictions for all processes $e^+e^- \rightarrow 4$ fermions + gamma,” *Nucl. Phys. B* **560** (1999) 33–65, arXiv:hep-ph/9904472
- [42] A. Denner, S. Dittmaier, M. Roth, and L. H. Wieders, “Electroweak corrections to charged-current $e^+e^- \rightarrow 4$ fermion processes: Technical details and further results,” *Nucl. Phys. B* **724** (2005) 247–294, arXiv:hep-ph/0505042. [Erratum: Nucl.Phys.B 854, 504–507 (2012)]
- [43] A. Denner and S. Dittmaier, “The Complex-mass scheme for perturbative calculations with unstable particles,” *Nucl. Phys. B Proc. Suppl.* **160** (2006) 22–26, arXiv:hep-ph/0605312
- [44] T. Hahn and M. Perez-Victoria, “Automatized one loop calculations in four-dimensions and D-dimensions,” *Comput. Phys. Commun.* **118** (1999) 153–165, arXiv:hep-ph/9807565
- [45] T. Hahn, “CUBA: A Library for multidimensional numerical integration,” *Comput. Phys. Commun.* **168** (2005) 78–95, arXiv:hep-ph/0404043
- [46] R. Frederix, T. Gehrmann, and N. Greiner, “Automation of the Dipole Subtraction Method in MadGraph/MadEvent,” *JHEP* **09** (2008) 122, arXiv:0808.2128 [hep-ph]
- [47] T. Gehrmann and N. Greiner, “Photon Radiation with MadDipole,” *JHEP* **12** (2010) 050, arXiv:1011.0321 [hep-ph]
- [48] S. Catani, Y. L. Dokshitzer, and B. R. Webber, “The K^- perpendicular clustering algorithm for jets in deep inelastic scattering and hadron collisions,” *Phys. Lett. B* **285** (1992) 291–299
- [49] S. D. Ellis and D. E. Soper, “Successive combination jet algorithm for hadron collisions,” *Phys. Rev. D* **48** (1993) 3160–3166, arXiv:hep-ph/9305266
- [50] G. C. Blazey *et al.*, “Run II jet physics,” in *Physics at Run II: QCD and Weak Boson Physics Workshop: Final General Meeting*, pp. 47–77. arXiv:hep-ex/0005012
- [51] A. Denner, S. Dittmaier, M. Roth, and M. M. Weber, “Electroweak radiative corrections to $e^+e^- \rightarrow t\bar{t}H$,” *Phys. Lett. B* **575** (2003) 290–299, arXiv:hep-ph/0307193
- [52] A. Denner, S. Dittmaier, M. Roth, and M. M. Weber, “Electroweak corrections to $e^+e^- \rightarrow f \text{ anti-}f H$,” *Nucl. Phys. B Proc. Suppl.* **135** (2004) 88–91, arXiv:hep-ph/0406335
- [53] T. Plehn, D. L. Rainwater, and D. Zeppenfeld, “Determining the Structure of Higgs Couplings at the LHC,” *Phys. Rev. Lett.* **88** (2002) 051801, arXiv:hep-ph/0105325
- [54] S. S. Biswal, R. M. Godbole, B. Mellado, and S. Raychaudhuri, “Azimuthal Angle Probe of Anomalous HWW Couplings at a High Energy ep Collider,” *Phys. Rev. Lett.* **109** (2012) 261801, arXiv:1203.6285 [hep-ph].